Experimental Techniques (2022) 46:273–286
https://doi.org/10.1007/s40799-021-00476-y

RESEARCH PAPER

Two-Dimensional Meshfree-Based Digital Image Correlation for Strain-Displacement Measurement

S.H. Drahman[1] · A.R. Zainal Abidin[2] · A.B.H. Kueh[3]

Received: 14 March 2020 / Accepted: 20 April 2021 / Published online: 18 May 2021

Abstract
At present, there are various image registration algorithms under active development for digital image correlation techniques. These techniques include the meshfree-based (MFree-based) digital image correlation. However, there exists very little study in advancing the method for better computational efficiency in engineering measurement applications. Also, a comparative investigation against the more well-known finite element-based digital image correlation is absent. This paper presents the development of an efficient two-dimensional (2D) MFree-based digital image correlation technique to obtain the strain and displacement of a planar object. In the present method, the speckle pattern in the form of circular adhesive markers is first detected and tracked by employing the Circular-Hough-Transform and Kanade-Lucas-Tomasi algorithms. The element-free Galerkin approach that specifically employs the moving least-square approximation has been adopted as the meshfree method for the strain and displacement determination. A series of tensile tests on pure epoxy samples has then been carried out to verify the applicability of the proposed 2D MFree-based digital image correlation technique, from which a good agreement of the strain and displacement description is found when compared with that obtained by the conventional strain gauge method. Furthermore, the full-field deformations computed from the ABAQUS model have been well captured by the proposed technique. This concludes that the proposed 2D MFree-based digital image correlation technique is greatly applicable and is recommended for use in determining the planar material engineering properties.

Keywords Digital image correlation · Meshfree · Element-free Galerkin · Circular-Hough-transform algorithm · Kanade-Lucas-Tomasi algorithm · Planar strain

Introduction

Non-invasive approaches like videogrammetry and photogrammetry are fast becoming the better-accepted laboratory and field measurement options encompassing all scientific and engineering areas. As the name implies, non-invasive measurement methods rely greatly on the detection of geolocations of points of interest on specimens with little or no attached gauging device on them to ascertain an unobstructed tracking of these points, especially during the deformation state. These methods become desirably useful particularly at the stages nearing, during, and after the occurrence of a failure in specimens, at which any attached measuring device may no longer fully functional or registering erroneous reading at the points of interest. In general, the existing non-invasive measurement approaches employ the digital image correlation (DIC) concept as their fundamental working template. DIC is a non-contact measurement method used to determine the full-field shape, deformation, and motion of an object with the aid of optical tools [1, 2]. Its popularity in both academic and industrial applications, such as measurement of object deformation [3, 4]; structural health monitoring, maintenance, and process control [5–7]; material defects detection [8, 9]; biological tissues and biomaterials deformations tracking [10–12], etc., roots in its versatility and flexibility. The basic principle and development of DIC since its establishment in 1982 [13] until 2018 have been remarkably reviewed in a recent paper by Pan [14]. Generally, DIC techniques require

✉ A.R. Zainal Abidin
arazin@utm.my

[1] Faculty of Science and Technology, i-CATS University College, 93350 Kuching, Sarawak, Malaysia

[2] School of Civil Engineering, Faculty of Engineering, Universiti Teknologi Malaysia, UTM, 81310 Johor Bahru, Malaysia

[3] Department of Civil Engineering, Faculty of Engineering, Universiti Malaysia Sarawak, 94300 Kota Samarahan, Sarawak, Malaysia

first the speckle pattern fabrication, then the digital image acquisition, and finally the post-processing of images to obtain the measurement of deformation [2, 14]. It is common knowledge that the use of the DIC technique is costly due to the high price of the employed optical tools, especially when using the bilateral telecentric lens [15]. However, with rapidly advancing technologies nowadays, the DIC technique has made itself available in a more cost-effective platform, i.e., smartphones [16–19]. Therefore, the application of the DIC technique is becoming more desirable in scientific works than the conventional and more invasive sensors such as strain gauges.

The DIC method can be carried out either in a two-dimensional (2D) or three-dimensional (3D) setup. The 2D DIC is particularly useful in capturing the in-plane deformation of an object. However, previous works have found that the out-of-plane deformation can adversely affect the accuracy of the measurement, and the higher-level 3D DIC techniques are, therefore, recommended [20, 21]. Nonetheless, the 2D DIC techniques are still extensively used in the measurement of the fundamental deformation states of a planar object under various testing methods, such as tension [22–25], compression [23, 26, 27], bending [23, 28], and vibration [29–31], to name a few. Besides that, several attempts have been made to solve the out-of-plane effects of the 2D DIC techniques, e.g., the compensation methods [32, 33], the combination of 2D DIC with two parallel planar lasers [34], the self-correction method [35], etc.

In the implementation of DIC, various factors could contribute to its accuracy. These include speckle patterns, subpixel interpolation and algorithm, subset size, as well as image or video resolution and noise [36, 37]. For a study of the subset size effect, Pan et al. (2008) found that a small subset size of the image with high contrast will contribute to a more accurate reading of deformation [37]. Reu et al. [38] studied the loss of image resolution of the camera system due to the aperture and found that it can be overcome by increasing the speckle size or subset size. Different speckle pattern fabrications adopted in previous works like natural and artificial speckle patterns have been well summarized by Dong and Pan [2]. Several notable approaches to fabricate the speckle patterns are spray paints [39], printed-speckle patterns [40], two straight lines markers [41], circular adhesive markers [19], etc. By employing the latter two approaches, the strain or real displacement-time at the points of interest can be measured from the directly marked targets on the sample surface before executing the experimental work. Moreover, these approaches use a small coverage of speckle patterns compared to the commonly used spray paints, which result in better computational efficiency during the post-processing of the images.

In the DIC technique, the use of algorithms is essential in the post-processing of images. Various image registration algorithms have been developed for the DIC technique over the last three decades, from which the most commonly employed are the subset-based DIC and finite element-based (FE-based) DIC [42, 43]. The global FE-based DIC has an advantage over local subset-based DIC due to its deformation continuity formulation [42, 44]. A more recent image registration algorithm for the global deformation measurement is the meshfree-based (MFree-based) DIC, which was introduced by Andrianopoulos utilizing the element-free Galerkin (EFG) method in 2006 [45]. This method is relatively easier to adopt with high accuracy compared to the FE-based DIC due to the meshless feature of the MFree method. In the following years, a different variant of the method, the mesh-free random grid method, has since been employed for the full-field strain measurement [46, 47].

Even though there exist some prior works on the use of the MFree method in the development of DIC, to the authors' knowledge, their amount is significantly little, remain at the infancy stage while have yet been well-developed for better computational cost- and time-efficiencies in the DIC application. In the present paper, we, therefore, propose the MFree-based 2D DIC measurement technique incorporating the speckle pattern fabrication method by means of circular adhesive markers intended for use via the digital camera equipped with the common specification. The MFree method used is based on the EFG formulation. Also, the 2D DIC setup is employed as it is adequate for validating the fundamental deformation states of the coupon tests in a laboratory experimental setting. The aim is to provide a simple yet computationally efficient technique in determining the principal material properties commonly desired at the initial phases of engineering analyses and designs. This can be realized through the experimental works via the basic static tensile test, which is also presented in this paper. Granted there is a dense population of image-derived measurement methods in scholastic literature, it is worthwhile to appreciate that the novelty of the current work is on the use of a meshfree method to forecast the displacement/strain field variables. Driven by the capability of the interpolation features of the meshfree method, fewer nodes are expected in characterizing the spatial continuity of the displacement/strain field. This is specifically useful in the presence of insufficient data points from the measurement. As far as research works are concerned, it is always beneficial to venture into new ideas to explore new possibilities as well as to complement the existing methods where appropriate. It is worth noting that the proposed method is focused on a low-cost variant of DIC with the limitation of no location dependency and is specifically developed for a 2D plane stress elastic analysis, in which the strain orthogonal to force is not considered.

The remainder of the paper is arranged as follows. Section 2 elaborates the principle of the proposed method incorporating the direct utilization of MATLAB's toolboxes and built-in functions. Section 3 deals with the static

experimental works, namely, tensile tests to demonstrate the application of the developed MFree-based DIC method. The results and discussion for the strains obtained using the DIC technique and its verification with those measured using strain gauge are presented in Section 4. Lastly, Section 5 offers the concluding remarks of the main findings of the paper.

Development of the Proposed Method

Before the commencement of the experimental tests, the speckle pattern fabrication on the specimen planar surface is carried out. The overall post-processes of the recorded images involve the use of the commercially available software, MATLAB. First, the speckle patterns are detected, calibrated, and tracked by using MATLAB's toolboxes. Descriptions of these steps are presented in the following section. Then, the EFG approach is used to determine the full-field strain and the strain at the points of interest. Since this work is devoted to the videogrammetry application, the strains are obtained every second from the beginning of the testing until the failure of the specimens.

Speckle Pattern Detection, Calibration, and Tracking

Instead of using the commonly employed speckle pattern (i.e., randomly distributed artificial speckle patterns produced from spray paint), this paper proposes a regularly distributed speckle pattern using a set of circular adhesive markers of constant size, as shown in Fig. 1. These markers are then detected by utilizing the image processing toolbox of the MATLAB software through the *imfindcircles* function. This function implements the Circular Hough Transform (CHT) algorithm to find and detect the circular markers in images. The coordinates of each centroid are determined and represented as the field nodes.

In the next step, a calibration of the image pixels is performed based on the real measurement unit. The calibration is executed in terms of the scale factor, k, as given by:

$$k = \frac{R_A}{R_P} \tag{1}$$

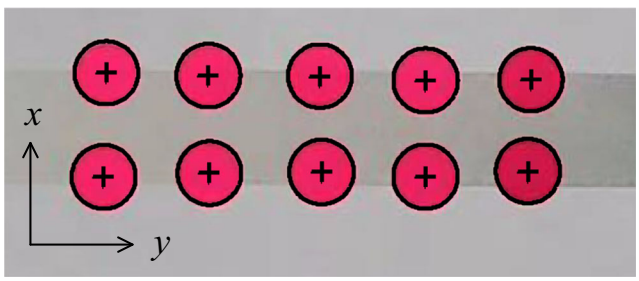

Fig. 1 Speckle pattern detection using the CHT algorithm (+ denotes the center of the circular adhesive markers) via the MATLAB software

The image pixels of the speckle pattern radius, R_P, can be obtained directly from the *imfindcircles* function whereas the actual radius of the circular adhesive marker, R_A, is usually given readily on its manufacturer's packaging or measured directly from the marker. After the k value is determined, one can obtain the magnitude of the actual deformation by multiplying the digitally obtained deformation in pixels with the k value.

The speckle pattern tracking utilizes the Kanade-Lucas-Tomasi (KLT) algorithm in the MATLAB software, particularly, by employing the computer vision toolbox, the syntax of which is *vision.PointTracker* [48]. The purpose is to track the speckle pattern movement, in terms of coordinates, every frame per second (fps) of the recorded video clip. The captured video should show all the speckle patterns from the exact starting time of the object when subjected to load until it breaks or fails. Figure 2 shows the speckle patterns movement when the object is pulled in the y-direction. Using the algorithm, the displacements both in the x- and y-directions of the field nodes can be obtained.

MFree-Based 2D DIC Measurement Technique

From the determined nodal values, an MFree method is next used to interpolate the displacements field of the domain. Unlike the finite element approach that requires a predefined element connectivity for all elements used in the system, the MFree formulation operates on randomly scattered nodes within a domain of interest. Due to its flexibility in dealing with arbitrarily distributed nodes, the irregularity of the arrangement of the markers on the measured sample does not inflict any issue. This study employs the EFG method [49] to demonstrate the applicability of such a method to produce interpolated displacements field function over a domain while noting that any other available MFree methods can also be used for a similar purpose.

MFree Displacement Interpolation

The interpolation function of the EFG method over a domain is based on a simple representation of the shape function, $\phi(\mathbf{x})$, and the degree of freedom (DOF), u, given by:

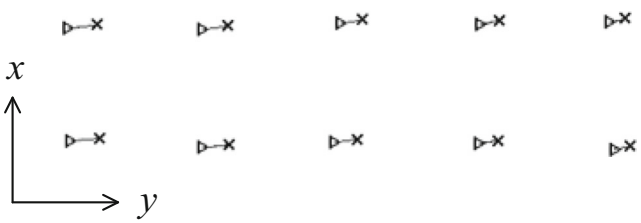

Fig. 2 Speckle patterns tracking using the KLT algorithm (▷ represents the undeformed node while × is that of deformed) via the MATLAB software

$$u^h(\mathbf{x}) = \sum_{i=1}^{n} \phi_i(\mathbf{x}) u_i = \mathbf{\Phi u} \tag{2}$$

in which $u^h(\mathbf{x})$ is the interpolation function, i is the running number of nodes, n is the number of nodes, $\mathbf{x}$ contains the (x, y) coordinates of the points of interest. This expression can also be written in a matrix form such that $\mathbf{\Phi}$is the shape function matrix for all i-th nodes as given by:

$$\mathbf{\Phi} = \{\phi_1(\mathbf{x}) \;\; \phi_2(\mathbf{x}), \ldots, \;\; \phi_n(\mathbf{x})\}^{\mathrm{T}} \tag{3}$$

and $\mathbf{u}$ is the vector of all DOFs:

$$\mathbf{u} = \{u_1 \;\; u_2, \ldots, \;\; u_n\}^{\mathrm{T}} \tag{4}$$

To maintain the locality of the interpolated field function, a local support domain is often used as shown in Fig. 3. This small domain controls the number of nodes being considered in Eq. (2) such that the influence of other nodes outside the domain is ignored. A support domain can be in any shape, but a circular domain is more common and convenient as far as the computer algorithm is concerned.

One of the important considerations in MFree methods that differentiates them from one another is the technique in determining the shape function. For the EFG method, a moving least-square (MLS) approximation is adopted, which is based on a fitting-curve technique commonly used in the statistical analysis [50, 51].

Shape Function by MLS Approximation

The development of a shape function via the MLS approximation initiates with a basic polynomial description:

$$u^h(\mathbf{x}) = \sum_{j=1}^{m} p_j(\mathbf{x}) a_j(\mathbf{x}) = \mathbf{p}^{\mathbf{T}}(\mathbf{x}) \mathbf{a}(\mathbf{x}) \tag{5}$$

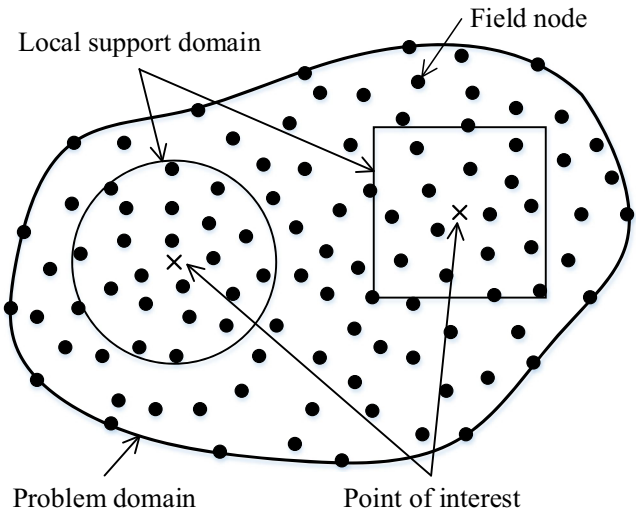

Fig. 3 Local support domains

where $u^h(\mathbf{x})$ is the displacement function similar to Eq. (2), $p_j(\mathbf{x})$ is the polynomial basis function, $a_j(\mathbf{x})$ represents the coefficients of $p_j(\mathbf{x})$, which are the unknowns, j is the running index, and m is the number of terms. Again, the expression can be written in matrix forms of $\mathbf{p}^{\mathbf{T}}(\mathbf{x})$ and $\mathbf{a}(\mathbf{x})$, as defined by Eqs. (6) and Eq. (7), respectively.

$$\mathbf{p}^{\mathbf{T}}(\mathbf{x}) = \begin{Bmatrix} 1 & x & y & x^2 & xy & y^2 & \ldots & x^p & y^p \end{Bmatrix} \tag{6}$$

$$\mathbf{a}(\mathbf{x}) = \{a_0(\mathbf{x}) \;\; a_1(\mathbf{x}) \;\; a_2(\mathbf{x}) \;\; \ldots \;\; a_k(\mathbf{x})\} \tag{7}$$

Note that $\mathbf{p}^{\mathbf{T}}(\mathbf{x})$ is obtained by considering the Pascal triangle. Given a set of nodes at positions $\mathbf{x}_1$, $\mathbf{x}_2$, $\cdots$, $\mathbf{x}_n$ (n is the number of nodes) or $\mathbf{x}_i$, the interpolated field function values at the nodes can be evaluated as:

$$u^{h'}(\mathbf{x}_i) = \mathbf{p}^{\mathbf{T}}(\mathbf{x}_i)\mathbf{a}(\mathbf{x}), \quad i = 1, 2, \ldots, n \tag{8}$$

If the actual nodal values are given by u_i, a functional of weighted residuals of the expression can be constructed as:

$$\Delta = \sum_{i=1}^{n} w(\mathbf{x}-\mathbf{x}_i)\left[u^h(\mathbf{x}_i)-u_i\right]^2 \tag{9}$$

with $w(\mathbf{x}-\mathbf{x}_i)$ being the weight function, defined by [49]:

$$w(\mathbf{x}-\mathbf{x}_i) = w\left(\overline{d}\right) = \begin{cases} \dfrac{\exp\left[-\left(\overline{d}/c\right)^{2k}\right]-\exp\left[-(r/c)^{2k}\right]}{1-\exp\left[-(r/c)^{2k}\right]}, & 0 \le \overline{d} \le r \\ 0, & \overline{d} > r \end{cases} \tag{10}$$

where r is the radius of the support domain, $\overline{d}$ is the distance between the centers of the support domain, $\mathbf{x}$ and $\mathbf{x}_i$, k, and c are constants that control the shape of the function. By substituting Eq. (5) into Eq. (9), we obtain:

$$\Delta = \sum_{i=1}^{n} w(\mathbf{x}-\mathbf{x}_i)\left[\mathbf{p}^{\mathbf{T}}(\mathbf{x}_i)\mathbf{a}(\mathbf{x})-u_i\right]^2 \tag{11}$$

Furthermore, minimizing the functional over $\mathbf{a}(\mathbf{x})$ gives:

$$\frac{\partial \Delta}{\partial \mathbf{a}(\mathbf{x})} = 0 \tag{12}$$

such that

$$\underbrace{\sum_{i=1}^{n} w(\mathbf{x}-\mathbf{x}_i)\mathbf{p}(\mathbf{x}_i)\mathbf{p}^{\mathbf{T}}(\mathbf{x}_i)}_{\mathbf{A}(\mathbf{x})} \mathbf{a}(\mathbf{x}) = \underbrace{w(\mathbf{x}-\mathbf{x}_i)\mathbf{p}(\mathbf{x}_i)}_{\mathbf{B}(\mathbf{x})} \mathbf{u} \tag{13}$$

and

$$\mathbf{a}(\mathbf{x}) = \mathbf{A}^{-1}(\mathbf{x})\,\mathbf{B}(\mathbf{x})\,\mathbf{u} \tag{14}$$

By substituting Eq. (14) into Eq. (5), the following equation can be acquired:

$$\begin{aligned} u^h(\mathbf{x}) &= \sum_{j=1}^{m} p_j(\mathbf{x}) a_j(\mathbf{x}) \\ &= \sum_{i=1}^{n} \underbrace{\sum_{j=1}^{m} p_j(\mathbf{x}) \left(\mathbf{A}^{-1}(\mathbf{x})\mathbf{B}(\mathbf{x})\right)_{ji}}_{\phi_i(\mathbf{x})} u_i \\ &= \sum_{i=1}^{n} \phi_i(\mathbf{x})\, u_i \end{aligned} \tag{15}$$

in which $\phi_i(x)$ is the MLS shape function that will be adopted in Eq. (2).

Displacements Field for Planar Analysis

Since there are two components of displacement in the x- and y-directions in a general plane stress problem, Eq. (2) can be adopted to represent both fields:

$$\begin{aligned} u^h(\mathbf{x}) &= \sum_{i}^{n} \phi_i(\mathbf{x}) u_i \\ v^h(\mathbf{x}) &= \sum_{i}^{n} \phi_i(\mathbf{x}) v_i \end{aligned} \tag{16}$$

or they can be written in matrix forms as:

$$u^h = \begin{Bmatrix} u \\ v \end{Bmatrix}^h = \sum_{i=1}^{n} \underbrace{\begin{bmatrix} \phi_i & 0 \\ 0 & \phi_i \end{bmatrix}}_{\mathbf{\Phi}_i} \underbrace{\begin{Bmatrix} u_i \\ v_i \end{Bmatrix}}_{\mathbf{u}_i} = \sum_{i=1}^{n} \mathbf{\Phi}_i \mathbf{u}_i \tag{17}$$

where u and v represent horizontal and vertical displacements, respectively. The displacement field is now established over the domain of interest and displacements at any location can simply be interpolated using Eq. (17).

Determination of the Strain Field

Having established the displacements field function over a domain by Eq. (2), the strain field function, $\varepsilon^h(\mathbf{x})$, can also be obtained by the partial derivatives given as:

$$\begin{aligned} \varepsilon^h(\mathbf{x}) &= \begin{Bmatrix} \varepsilon_x \\ \varepsilon_y \\ \varepsilon_{xy} \end{Bmatrix} = \begin{Bmatrix} \dfrac{\partial u}{\partial x} \\ \dfrac{\partial v}{\partial y} \\ \dfrac{\partial v}{\partial y} + \dfrac{\partial u}{\partial x} \end{Bmatrix} \\ &= \begin{bmatrix} \dfrac{\partial}{\partial x} & 0 \\ 0 & \dfrac{\partial}{\partial y} \\ \dfrac{\partial}{\partial y} & \dfrac{\partial}{\partial x} \end{bmatrix} \begin{Bmatrix} u \\ v \end{Bmatrix}^h = \mathbf{L} u^h \end{aligned} \tag{18}$$

where $\mathbf{L}$ is the differential operator matrix. By considering Eq. (17) in Eq. (18), the strain field function can be further expressed as:

$$\begin{aligned} \boldsymbol{\varepsilon}^h(\mathbf{x}) &= \sum_{i=1}^{n} \begin{bmatrix} \dfrac{\partial}{\partial x} & 0 \\ 0 & \dfrac{\partial}{\partial y} \\ \dfrac{\partial}{\partial y} & \dfrac{\partial}{\partial x} \end{bmatrix} \begin{bmatrix} \phi_i & 0 \\ 0 & \phi_i \end{bmatrix} \begin{Bmatrix} u_i \\ v_i \end{Bmatrix} \\ &= \sum_{i=1}^{n} \begin{bmatrix} \dfrac{\partial \phi_i}{\partial x} & 0 \\ 0 & \dfrac{\partial \phi_i}{\partial y} \\ \dfrac{\partial \phi_i}{\partial y} & \dfrac{\partial \phi_i}{\partial x} \end{bmatrix} \begin{Bmatrix} u_i \\ v_i \end{Bmatrix} \end{aligned} \tag{19}$$

Therefore, the strain equation can be written as:

$$\boldsymbol{\varepsilon}^h = \sum_{i=1}^{n} \mathbf{\Gamma}_i \mathbf{u}_i \tag{20}$$

where

$$\mathbf{\Gamma}_i = \begin{bmatrix} \dfrac{\partial \phi_i}{\partial x} & 0 \\ 0 & \dfrac{\partial \phi_i}{\partial y} \\ \dfrac{\partial \phi_i}{\partial y} & \dfrac{\partial \phi_i}{\partial x} \end{bmatrix} \tag{21}$$

Note that, to evaluate strain at any position of $\mathbf{x}$, the first derivatives of the MLS shape function in both x- and y-directions are required, the detailed calculation of which can be found in [49]. In this study, the value of strain is evaluated in the middle of the sample for comparison with the experimental data measured using a strain gauge, and also at several points over the sample for the strain contours plotting purposes, as shown in Fig. 4.

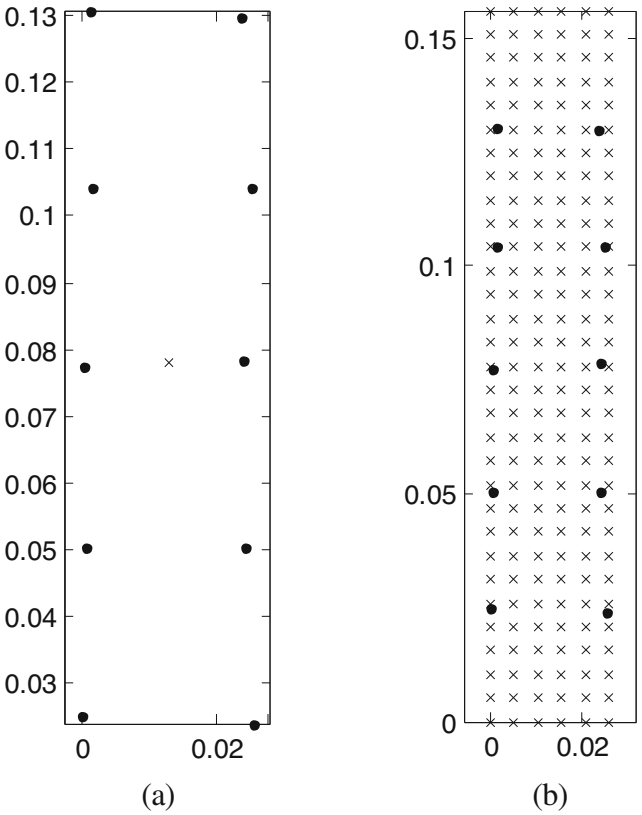

Fig. 4 Strain measurement using the EFG method showing evaluated nodes for determining (**a**) strain in the middle of the sample and (**b**) full-field strain measurement (• represents the speckle pattern or circular adhesive markers while × designates the point of interest)

Experiments

Material and Sample Preparation

The samples for the tensile test were prepared based on the BS EN ISO 527-1:2012 and BS EN ISO 527-2:2012 standards. The samples were made from the EP-1006 epoxy resin with a mixture of resin (62.5%) and its hardener (37.5%). The resin and its hardener were mixed and stirred as homogeneous as possible for about 5 min before the mixture was poured into a mold. Then, the sample was cured for at least 48 h at room temperature (as recommended by the manufacturer, S&N Chemicals Sdn. Bhd). The cured sample is shown in Fig. 5(a). A pair of aluminum plates were installed sandwiching the sample at each gripped region to provide a better grip between the sample and the tensile machine. Then, the speckle pattern (i.e., circular adhesive markers) was constructed on the surface of the sample. The adopted marker size was 6 mm. In general, any marker size is employable on the condition that it fits the sample's surface while positioned within the boundary of the image frame. The location of the markers can be randomly distributed over the domain of interest as long as they are attached properly to the sample. To allow for at least a linear interpolation of the displacements function, a minimum of two nodes over both horizontal and vertical directions need to be employed. In the calibration study, a tolerance of ±0.06 mm was considered. A strain gauge was installed unidirectionally on the other side of the same sample, as displayed in Fig. 5(b). The strain gauge was bonded to the sample surface using the instantly bonding industrial superglue. The strain gauges were supplied by Tokyo Sokki Kenkyujo Co., Ltd. The employed gauge length was 2 mm with a factor of 2.09 ± 1%. The gauge resistance and transverse sensitivity were 119.8 ± 0.5 Ω and 0.3%, respectively.

Experimental Test

Tensile Test

The schematic diagram of the tensile test and its setup using both strain gauge and DIC methods are shown in Fig. 6. The Instron 5567 tensile test machine with a maximum load

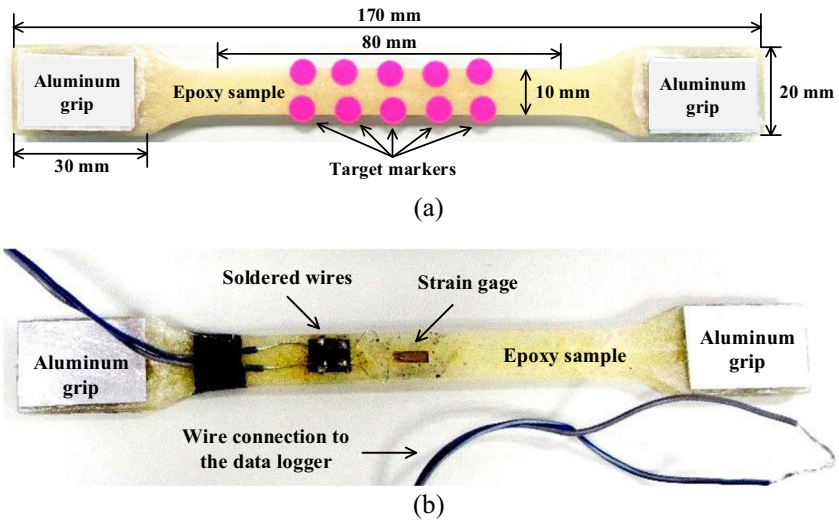

Fig. 5 Sample layout for tensile test for both DIC and strain gauge methods; (**a**) the sample with circular adhesive markers and (**b**) location of strain gauge on the flipped side of the sample

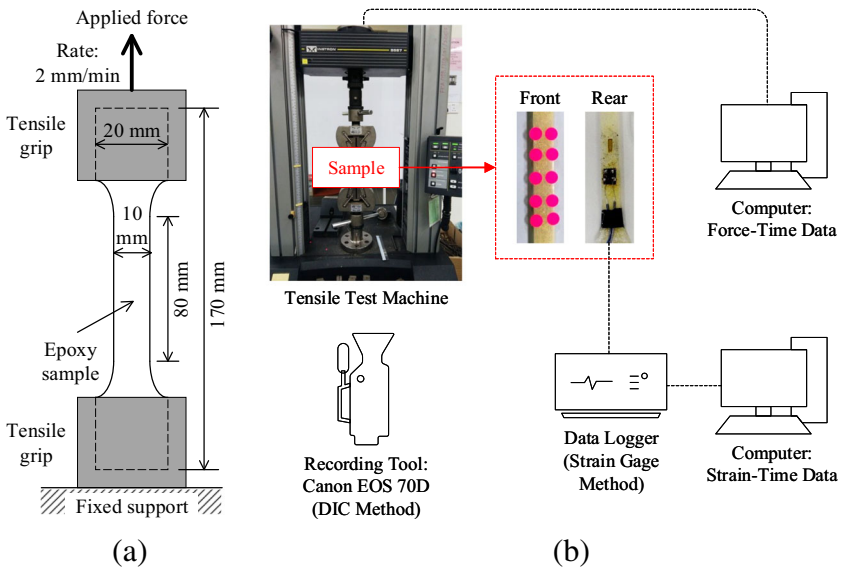

Fig. 6 **a** Schematic diagram of the tensile test and **b** the setup for tensile test using strain gauge and DIC methods

capacity of 50 kN was connected to the computer, in which the instantaneous loading level applied to the samples was displayed. Then, the strain gauge that was attached to the sample was connected via soldered wires to the data logger, which was connected to the computer for strain data recording. The rate used for the tensile test was 2 mm/min. The deformation of each sample due to stretching by the tensile machine was recorded using the digital camera, Canon EOS 70D, its lens of which was pointed to the sample. There was no specific distance between the camera and the sample by grounding on the condition that all speckle patterns appeared within the image frame. Additionally, the camera was set to the autofocus configuration to zoom-in only on the area of the sample equipped with the speckle patterns. Care had been taken to ensure that all the speckle patterns on the sample were fully displayed on the camera screen from the start to the end of the tensile test. It is important to emphasize that the camera lens should be perpendicularly aligned with the measured specimen surface to minimize any error in the strain determination. Also, the camera was first set to the resolution of 1280 × 720 with a capturing speed of 30 fps. Voice had been incorporated into the video clip as the signal to mark the initiation time of the test. The quality of the recorded speckle pattern movement plays an important role in determining the strain of the sample by the DIC method.

There were three outputs from the experimental works, i.e., force-time data, strain-time data, and video clip of the sample movement. The video clip was used in the DIC method to determine the strain of the sample. Once the strains from the DIC method were determined by synchronizing the test initiation time, they were plotted against time and compared with the strain-time data from the data logger. After the strain-time relationships of the DIC method were verified against those from the strain gauge, a series of stress-strain plots were produced to obtain the tensile modulus of the sample. The stress data was determined from the conversion of the force data from the computer connected to the tensile test machine.

Strain Measurement Procedure

The required strains for the current study were those in the direction parallel to the loading, i.e., longitudinal tensile strain. The video obtained from the tensile test was shortened by combining only the first frame per second for every one-second interval of the recorded video in order to accelerate the MATLAB running time for strain determination. For example, when the video time was 5 s with 30 fps, only images from the 1st, 31st, 61st, 91st, and 121st seconds were used in processing. This was performed by employing the *writeVideo* function in the MATLAB software.

After that, the CHT and KLT algorithms were programmed in MATLAB to detect and track the circular adhesive markers. These algorithms are readily available in MATLAB's toolboxes (see Section 2.1). Next, the proposed MFree-based 2D DIC measurement method (see Section 2.2) was coded in MATLAB to obtain the strain-time relationships of the samples in the *y*-direction. The strain-time relationships were obtained in the middle of the samples by interpolating the strains from the speckle pattern positions.

It should be noted here that there were several control parameters in the MATLAB source code along with the video resolution setting in successfully obtaining the best representation of strains. The control parameters were the radius, sensitivity, and edge intensity of the speckle patterns. These parameters were changeable depending on the quality of the recording tool and video properties. The tensile test was carried out using the same recording tool arrangement and consistent lighting exposure, where ambient lighting in the

laboratory was used. This was to ensure that the control parameters in the MATLAB source code were consistent throughout the strain determination for every sample.

To guarantee that the proposed method was applicable for the strain determination, verification with the strain from the data logger was performed. As mentioned earlier, the parameters in the MATLAB source code are also dependent on the video properties. Hence, to explore the effects of the video properties, the resolutions were varied. The original recorded resolution was 1280 × 720. Then, this video was converted to a variety of videos with different resolutions using the Freemake Video Converter software version 4.1.10.31 [52]. The resolutions examined were 720 × 576, 720 × 480, 640 × 480, 640 × 360, 320 × 240, and 240 × 180. The resolution with the strains closer to those measured by the data logger was selected and employed throughout the study for the strain determination. Also, the strains resulted from the DIC method were compared with an idealized model constructed in the FE-based commercialized software, ABAQUS software version 6.14–2 [53], for full-field strain observation.

Results and Discussion

Strain Measurement: DIC Vs. Strain Gauge

A series of strains, ε, measured for the pure epoxy samples as obtained from the strain gauge and DIC methods are plotted

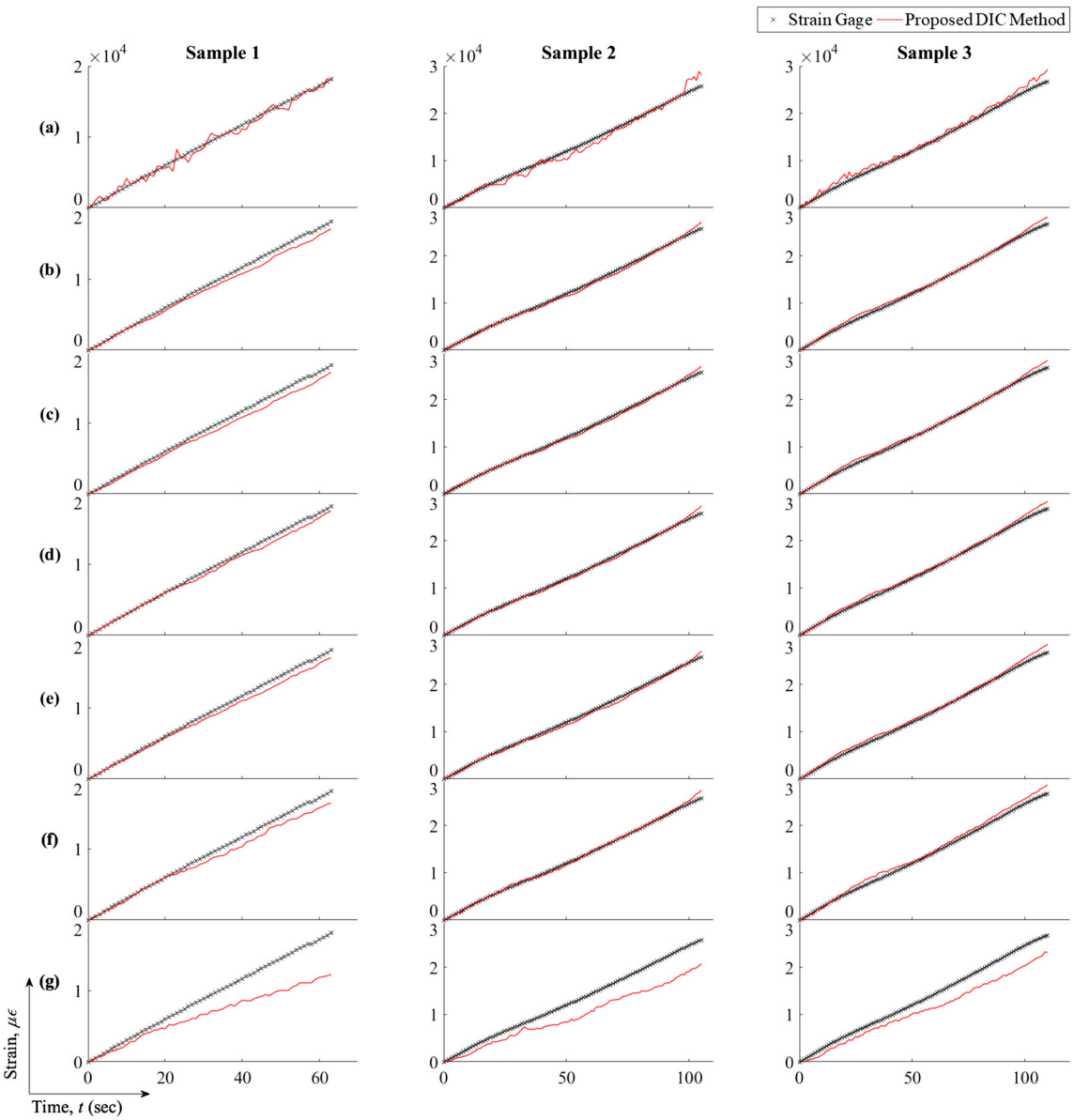

Fig. 7 Comparison of strain-time plots between strain gauge and DIC methods using different video resolutions; (**a**) original resolution (1280 × 720), (**b**) 720 × 576, (**c**) 720 × 480, (**d**) 640 × 480, (**e**) 640 × 360, (**f**) 320 × 240, and (**g**) 240 × 180

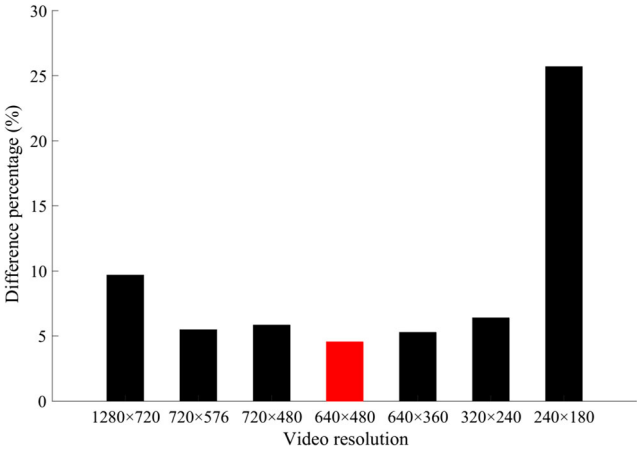

Fig. 8 Percentage of difference of strains for different video resolutions compared with the strain gauge method

against time, t, as shown in Fig. 7. There are in total three samples of pure epoxy with seven different video resolutions for each sample for comparison with the strains obtained from the strain gauge. From the graphs, it can be visually seen that the strains determined from the original video resolution (1280 × 720) fluctuate about the curve produced by the strain gauge, although its trend generally follows that of the strain gauge. Also, the strains for the smallest video resolution (240 × 180) deviate far away from the strain gauge data. The patterns for strains for video resolutions of 720 × 576, 720 × 480, 640 × 480, 640 × 360, and 320 × 240 are rather smooth while following, in general, those from the strain gauge.

Figure 8 shows the percentage of difference between strains from each video resolution and those measured by the strain gauge. It is obvious that the lowest video resolution (240 × 180) shows the highest difference percentage, which contributes to the highest inaccuracy. Also, the second-highest difference percentage is found for the original video resolution (1280 × 720). It has been determined that the difference percentages for video resolutions of 720 × 576, 720 × 480, 640 × 480, 640 × 360, and 320 × 240 are almost the same, but the lowest is exhibited by the red-colored bar with the video resolution of 640 × 480. Therefore, the video resolution of 640 × 480 was selected to conduct further analyses in determining the strain distribution of the epoxy samples. In general, it can be observed that the decrease in the original resolution down to 640 × 480 implies an increase in accuracy, which can be attributed to the reduction of noise in the video in conjunction with the decrease of the video pixel. However, it is shown that the conversion of resolution much lower than that reduces the accuracy of the strain data, which can be attributed to the loss of video information causing an error in the speckle patterns detection and movement tracking processes. By closely inspecting Fig. 8, it can be generally noticed that there exists an enhancement in measurement error at the adopted resolution departs further from 640 × 480, indicating clearly that there is an optimum video quality for the DIC method. Hence, a variation in resolution in measurement is suggested in the initiation stage of the utilization of this method.

Having decided on the best video resolution for the strain description, the determination of the tensile modulus for the pure epoxy samples was executed. Figure 9 shows the graphs of stress, σ, against strain, ε, for pure epoxy samples determined via both strain gauge and DIC methods. The straight lines were drawn at the initial part of the curves to compute the linear elastic relationship between stress and strain. The gradient of the linear function was adopted to determine the tensile modulus of the sample. The measured tensile modulus for this study was defined at its elastic state.

The details of the ultimate strength, σ_{ult}, and the strain at failure, ε_f, as well as the tensile modulus, E, obtained via both strain gauge and DIC methods for the pure epoxy samples are summarized in Table 1. The average σ_{ult} is 39.09 MPa. Also, the average ε_f are 23,569.33 με and 24,408.04 $\mu\varepsilon$ determined from the strain gauge and DIC methods, respectively. The difference has been computed as only 3.56%. In addition, the average E acquired from the strain gauge and DIC methods are 2529.10 MPa and 2534.80 MPa, respectively, with only a small difference between them, which is 0.23%. From these observed differences, it is apparent that the DIC method is comparable to the strain gauge in finding the strains of samples and can be implemented in the tensile testing.

It should be emphasized here that E was obtained from the strain measured in the middle part of the samples for both strain gauge and DIC methods. Also, this measured E was treated as the global E for all the analyses of the epoxy samples in the next section. The middle part of the data was taken because the highest stresses commonly occur there. Next, it is also worthwhile to conduct the full-field strain distribution determination of the sample to further validate the DIC method. This verification can be done by comparing the full-field strain obtained from the DIC method with the commercialized software, such as ABAQUS, which has been chosen in the current study.

Full-Field Strain Measurement: MFree-Based DIC Vs FE ABAQUS Model

In ABAQUS, the input for E was taken from the measured E of the strain gauge. Before proceeding to the verification process, the mesh convergence study was conducted. Figure 10 shows the mesh convergence study for the pure epoxy model in ABAQUS at a tensile extension of 0.1157 mm, which was randomly selected within the elastic regime. As the number of elements increases, the lower the strains and the more uniform their distribution is. In other words, the strain converges for the model as the number of elements increases, as shown in

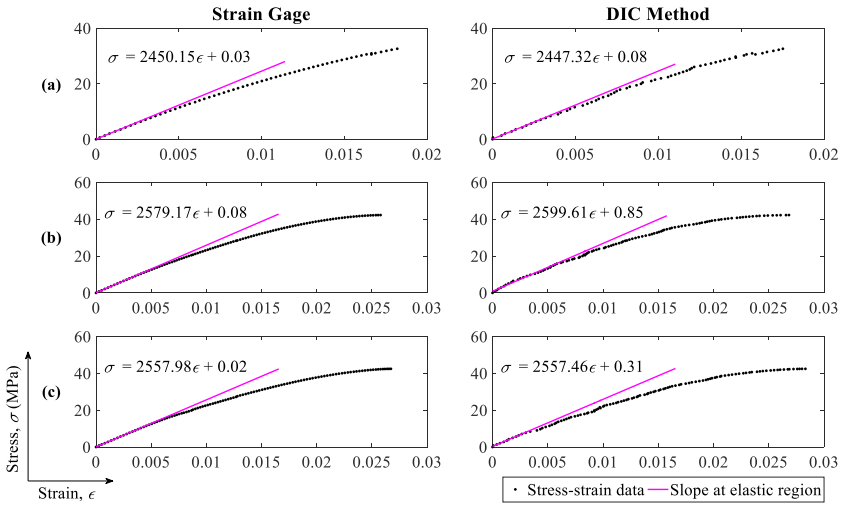

Fig. 9 Stress-strain plots of pure epoxy determined using the strain gauge and DIC methods for (**a**) Sample 1, (**b**) Sample 2, and (**c**) Sample 3

Table 1 Ultimate strength, strain at failure, and tensile modulus of pure epoxy samples

Pure Epoxy	Ultimate Strength, σ_{ult} (MPa)	Strain at Failure, ε_f ($\times 10^{-6}$)			Tensile Modulus, E (MPa)		
		Strain Gauge	Proposed DIC Method	Difference Percentage (%)	Strain Gauge	Proposed DIC Method	Difference Percentage(%)
Sample 1	32.59	18,199.00	17,515.97	3.75	2450.15	2447.32	0.12
Sample 2	42.24	25,786.00	27,395.68	6.24	2579.17	2599.61	0.79
Sample 3	42.43	26,723.00	28,312.48	5.95	2557.98	2557.46	0.02
Average	39.09	23,569.33	24,408.04	3.56	2529.10	2534.80	0.23

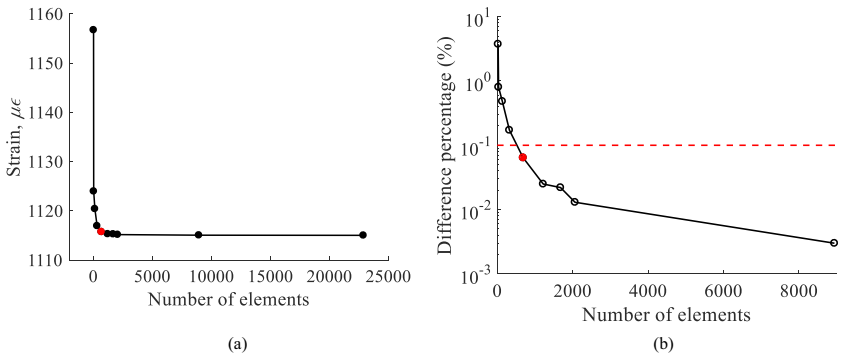

Fig. 10 Mesh convergence for pure epoxy model simulated by ABAQUS software at a tensile extension of 0.1157 mm; (**a**) strain vs. number of elements and (**b**) difference percentage of strain vs. number of elements

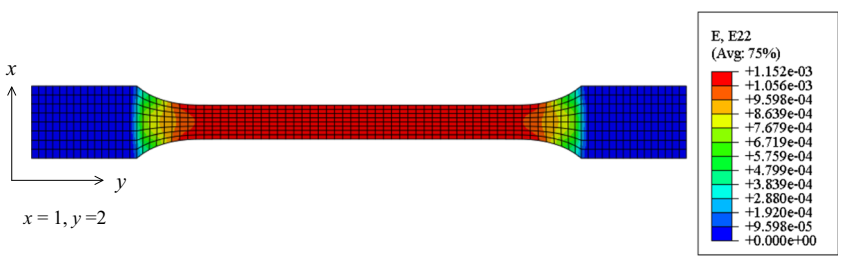

Fig. 11 Strain contour plot for an idealized pure epoxy model as simulated by the ABAQUS software at a tensile extension of 0.1157 mm

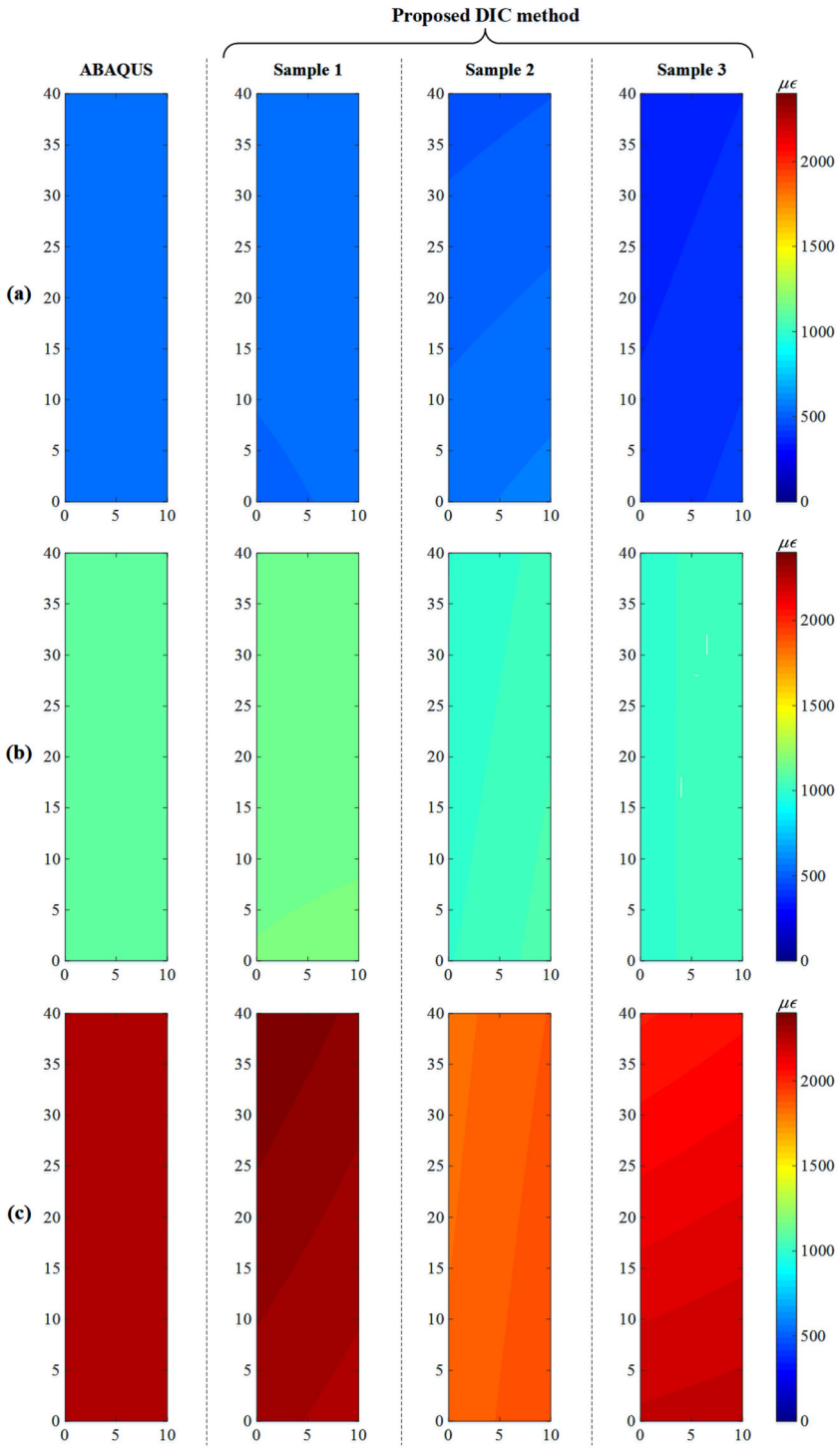

Fig. 12 Comparison of pure epoxy strain contours in the middle region of 10 × 40 mm size (width × length) of ABAQUS and the proposed DIC method (Samples 1, 2, and 3) at tensile extensions of (**a**) 0.0562 mm, (**b**) 0.1157 mm, and (**c**) 0.2338 mm

Fig. 10(a). Furthermore, the difference percentages of strain lesser than 0.1% can be observed begins at the fifth point as represented by the red dot in Fig. 10(b). These difference percentages show that 688 elements equivalent to a mesh of 8 × 86 can be used to conduct further analyses with a difference of only about 0.1% from the converged value.

The converged model as simulated by the ABAQUS software gives the ideal behavior of the pure epoxy sample under the tensile loading, as shown in Fig. 11. It can be noticed from the model that the strain distribution at the middle part of the model is of the same color, which means that the strains are, in general, the same throughout the region. Also, they are the highest strains experienced by the model. The strain

distribution in the middle part of the model, measuring to the dimensions of 10 × 40 mm (width × length), has been then focused and extracted out as the benchmarking comparative case with those obtained from the DIC method. Figure 12 shows the contour plots of the strain distribution obtained from the ABAQUS software and DIC method at tensile extensions of 0.0562 mm, 0.1157 mm, and 0.2338 mm, which are selected randomly in the range of the elastic regime of the stress-strain relationship.

It can be clearly seen that the strains increase with the tensile extensions, i.e., from 0.0562 mm to 0.2338 mm as shown in Fig. 12(a-c). The strains for tensile extensions of 0.0562 mm, 0.1157 mm, and 0.2338 mm are around 500 με, 1000 με, and 2000 με, respectively. Also, from Fig. 12, there exists a slight difference in colors in the contour plots, which means that the strain distributions are not uniform compared to those from ABAQUS. It is worth noting that this is common as it is difficult and nearly impossible to acquire an idealized strain distribution in reality. Furthermore, from the contour colors, the strains determined via the DIC method can be considered comparable with those obtained from ABAQUS. The slight change in contour coloration of the epoxy samples obtained by the DIC method may be attributed to the setting up process of samples on the Instron tensile test machine. This could result in a non-uniformity in the load distribution exerted by the tensile machine. Nonetheless, the differences are little. Having justified that, the strains determined by the DIC method are generally satisfying and comparable with those from ABAQUS.

Therefore, as a result of the verification of strains from the DIC method with both strain gauge and ABAQUS approaches, the currently proposed technique can be considered sufficiently accurate to be implemented in the tensile testing for the determination of strains.

Conclusions

This study proposed the two-dimensional meshfree-based digital image correlation technique, particularly, through the element-free Galerkin approach to measure the deformation of a planar object. This technique involved the speckle pattern production using the circular adhesive markers, which were then detected and tracked by employing the Circular Hough Transform and Kanade-Lucas-Tomasi algorithms, respectively. The displacement and strain of a planar object were determined based on the EFG method that employed the moving least-square approximation. To prove the applicability of the meshfree-based 2D DIC measurement technique, a series of tensile tests on pure epoxy samples were carried out. The determined strains were then verified with those obtained via the strain gauge. Seven different video resolutions were compared with those from the strain gauge, from which that of 640 × 480 exhibited the closest strain values with the lowest difference. Also, the difference percentages between the proposed technique and strain gauge method for strain at failure and tensile modulus of the samples were found to be only 3.56% and 0.23%, respectively. For the full-field strain measurement, the proposed technique was in good agreement with the outcomes computed from the ABAQUS model. The main benefits of the meshfree method can be appreciated through its capability to provide continuously interpolated displacement as well as strain functions coupled with a more relaxed requirement of only a few measured nodes, which is specifically useful in the situation when limited data points are available from the measurement. To summarize, the proposed MFree-based 2D DIC technique has demonstrated its high potential as a tool to measure the deformation of a planar object, from which its simplicity yet computationally efficient characteristics are the main attraction.

Acknowledgments The authors would like to acknowledge Universiti Teknologi Malaysia (UTM) for the financial supports through Research University Grant (GUP) (nos. 14 J21 and 19H41) for this research.

Funding Universiti Teknologi Malaysia (UTM) through GUP grants (nos. 14 J21 and 19H41).

Declarations

Conflicts of Interest/Competing Interests On behalf of all authors, the corresponding author states that there is no conflict of interest.

Abbreviation *2D,* two-dimensional; *3D,* three-dimensional; *CHT,* Circular-Hough-Transform algorithm; *DIC,* digital image correlation; *EFG,* element-free Galerkin; *FE,* finite element; *KLT,* Kanade-Lucas-Tomasi algorithm; *MFree,* meshfree; *MLS,* moving least-square

References

1. Sutton MA, Orteu JJ, Schreier HW (2009) Image correlation for shape, motion and deformation measurements. Springer Science+ Business Media, New York
2. Dong YL, Pan B (2017) A review of speckle pattern fabrication and assessment for digital image correlation. Exp Mech 57:1161–1181
3. Gencturk B, Hossain K, Kapadia A et al (2014) Use of digital image correlation technique in full-scale testing of prestressed concrete structures. Measurement 47:505–515
4. Sakanashi Y, Gungor S, Forsey AN, Bouchard PJ (2016) Measurement of creep deformation across welds in 316H stainless steel using digital image correlation. Exp Mech 57:231–244
5. Khadka A, Fick B, Afshar A et al (2020) Non-contact vibration monitoring of rotating wind turbines using a semi-autonomous UAV. Mech Syst Signal Process 138:1–14

6. Malesa M, Malowany K, Tomczak U et al (2013) Application of 3D digital image correlation in maintenance and process control in industry. Comput Ind 64:1301–1315
7. Hohmann BP, Bruck P, Esselman TC, et al (2013) The use of digital image correlation as a predictive maintenance tool for long-term operation of nuclear power plants. In: 9th International Conference on NDE in Relation to Structural Integrity for Nuclear and Pressurized Components. Washington, United States, pp 1044–1052
8. Holzmond O, Li X (2017) In situ real time defect detection of 3D printed parts. Addit Manuf 17:135–142
9. Scenini F, Azough F, Read-Jennings MCL, et al (2012) Use of digital image correlation (DIC) for detection of defects and monitoring of structural integrity in the nuclear industry. In: 9th International Conference on NDE in Relation to Structural Integrity for Nuclear and Pressurized Components. Washington, United States, pp 181–189
10. Genovese K (2019) An omnidirectional DIC system for dynamic strain measurement on soft biological tissues and organs. Opt Lasers Eng 116:6–18
11. Luyckx T, Verstraete M, De Roo K et al (2014) Digital image correlation as a tool for three-dimensional strain analysis in human tendon tissue. J Exp Orthop 1:1–9
12. Moerman KM, Holt CA, Evans SL, Simms CK (2009) Digital image correlation and finite element modelling as a method to determine mechanical properties of human soft tissue in vivo. J Biomech 42:1150–1153
13. Ranson WF, Peters WH (1982) Digital image techniques in experimental stress analysis. Opt Eng 21:427–431
14. Pan B (2018) Digital image correlation for surface deformation measurement: Historical developments, recent advances and future goals. Meas Sci Technol 29:082001
15. Pan B, Yu L, Wu D (2013) High-accuracy 2D digital image correlation measurements with bilateral telecentric lenses: error analysis and experimental verification. Exp Mech 53:1719–1733
16. Xie B, Zhao X, Li J, et al (2019) Research on 2D digital image correlation measurement based on smartphones. In: Proceedings of SPIE 10972 Health Monitoring of Structural and Biological Systems XIII. Colorado, United States, p 109722F
17. Vidvans A, Basu S (2018) Smartphone based scalable reverse engineering by digital image correlation. Opt Lasers Eng 102:126–135
18. Yu L, Tao R, Lubineau G (2019) Accurate 3D shape, displacement and deformation measurement using a smartphone. Sensors 19:1–19
19. Chih LY, Zainal Abidin AR, Kueh ABH (2017) Displacement measurement of structural response using matlab image processing and object. In: 2nd proceeding of civil engineering. Faculty of Civil Engineering Universiti, Universiti Teknologi Malaysia, Johor, pp 1–6
20. Sutton MA, Yan JH, Tiwari V et al (2008) The effect of out-of-plane motion on 2D and 3D digital image correlation measurements. Opt Lasers Eng 46:746–757
21. Haddadi H, Belhabib S (2008) Use of rigid-body motion for the investigation and estimation of the measurement errors related to digital image correlation technique. Opt Lasers Eng 46:185–196
22. Paul SK, Roy S, Sivaprasad S, Tarafder S (2019) Forming limit diagram generation from in-plane uniaxial and notch tensile test with local strain measurement through digital image correlation. Phys Mesomech 22:340–344
23. Bechle NJ, Kyriakides S (2014) Localization in NiTi tubes under bending. Int J Solids Struct 51:967–980
24. Cerbu C, Xu D, Wang H, Roşca IC (2018) The use of digital image correlation in determining the mechanical properties of materials. In: 3rd China-Romania Science and Technology Seminar (CRSTS 2018), IOP Conference Series: Materials Science and Engineering. Brasov, Romania, p 012007
25. Dong B, Tian L, Pan B (2019) Tensile testing of carbon fiber multifilament using an advanced video extensometer assisted by dual-reflector imaging. Measurement 138:325–331
26. Voiconi T, Linul E, Marşavina L et al (2014) Experimental determination of mechanical properties of aluminium foams using digital image correlation. Key Eng Mater 601:254–257
27. Caselle C, Umili G, Bonetto S et al (2019) Evolution of local strains under uniaxial compression in an anisotropic gypsum sample. In: National Conference of the researchers of geotechnical engineering. Springer, Cham, pp 454–461
28. Alipour M, Washlesky SJ, Harris DK (2019) Field deployment and laboratory evaluation of 2D digital image correlation for deflection sensing in complex environments. J Bridg Eng 24:1–15
29. Zappa E, Hasheminejad N (2017) Digital image correlation technique in dynamic applications on deformable targets. Exp Tech 41:377–387
30. Du W, Lei D, Bai P, et al (2020) Dynamic measurement of stay-cable force using digital image techniques. Measurement 151:107211
31. Caetano E, Silva S, Bateira J (2011) A vision system for vibration monitoring of civil engineering structures. Exp Tech 35:74–82
32. Pan B, Yu L, Wu D (2014) High-accuracy 2D digital image correlation measurements using low-cost imaging lenses: implementation of a generalized compensation method. Meas Sci Technol 25:025001
33. Wittevrongel L, Badaloni M, Balcaen R et al (2015) Evaluation of methodologies for compensation of out of plane motions in a 2D digital image correlation setup. Strain 51:357–369
34. Wang Z, Fang F, Liu B, Wang Z (2015) An experimental method for eliminating effect of rigid out-of-plane motion on 2D-DIC. Opt Lasers Eng 73:137–142
35. Yan W, Lin F (2016) Self-correction method of out-of-plane motions in two-dimensional digital image correlation. Proc Inst Mech Eng Part B J Eng Manuf 232:1672–1676
36. Chen Z, Shao X, Xu X, He X (2018) Optimized digital speckle patterns for digital image correlation by consideration of both accuracy and efficiency. Appl Opt 57:884–893
37. Pan B, Xie H, Wang Z et al (2008) Study on subset size selection in digital image correlation for speckle patterns. Opt Express 16:7037–7048
38. Reu PL, Sweatt W, Miller T, Fleming D (2015) Camera system resolution and its influence on digital image correlation. Exp Mech 55:9–25
39. Chu TC, Ranson WF, Sutton MA, Peters WH (1985) Applications of digital-image-correlation techniques to experimental mechanics. Exp Mech 25:232–244
40. Ashrafi M, Tuttle ME (2015) Measurement of strain gradients using digital image correlation by applying printed-speckle patterns. Exp Tech 40:891–897
41. Liljenhjerte J, Upadhyaya P, Kumar S (2016) Hyperelastic strain measurements and constitutive parameters identification of 3D printed soft polymers by image processing. Addit Manuf 11:40–48
42. Wang B, Pan B, Lubineau G (2015) Some practical considerations in finite element-based digital image correlation. Opt Lasers Eng 73:22–32
43. Wang B, Pan B (2016) Subset-based local vs. finite element-based global digital image correlation: a comparison study. Theor Appl Mech Lett 6:200–208
44. Sun Y, Pang JHL, Wong CK, Su F (2005) Finite element formulation for a digital image correlation method. Appl Opt 44:7357–7363
45. Andrianopoulos NP (2006) Full-field displacement measurement of a speckle grid by using a mesh-free deformation function. Strain 42:265–271

46. Iliopoulos AP, Michopoulos JG, Andrianopoulos NP (2009) Performance sensitivity analysis of the mesh-free random grid method for whole field strain measurements. In: Proceedings of the ASME 2008 International Design Engineering Technical Conferences & Computers and Information in Engineering Conference IDETC/CIE 2008. American Society of Mechanical Engineers, New York, United States, pp 545–555
47. Iliopoulos AP, Michopoulos JG (2009) Effects of anisotropy on the performance sensitivity of the mesh-free random grid method for whole field strain. In: Proceedings of the ASME 2009 International Design Engineering Technical Conferences & Computers and Information in Engineering Conference IDETC/CIE 2009. American Society of Mechanical Engineers, California, United States, pp 65–74
48. MathWorks (2012) vision.PointTracker. https://www.mathworks.com/help/vision/ref/vision.pointtracker-system-object.html. Accessed 12 Nov 2019
49. Belytschko T, Lu YY, Gu L (1994) Element-free Galerkin methods. Int J Numer Methods Eng 37:229–256
50. Lancaster P, Salkauskas K (1981) Surfaces generated by moving least squares methods. Math Comput 37:141–158
51. Cleveland WS (1993) Visualizing Data. Hobart Press, Murray Hill
52. Ellora Assets Corporation (2017) Freemake Video Converter [Computer software]
53. Dassault Systemes (2014) ABAQUS [Computer software]